



HAL
open science

Impact of Acidity and Metal Particle Size on the Competitive Pathways of Benzyl Phenyl Ether Conversion to Aromatics and Cycloalkanes in a Nonpolar Solvent

Raphaëla Azevedo Rafael, Robert Wojcieszak, Eric Marceau, Fabio Bellot Noronha

► To cite this version:

Raphaëla Azevedo Rafael, Robert Wojcieszak, Eric Marceau, Fabio Bellot Noronha. Impact of Acidity and Metal Particle Size on the Competitive Pathways of Benzyl Phenyl Ether Conversion to Aromatics and Cycloalkanes in a Nonpolar Solvent. *ACS Sustainable Chemistry & Engineering*, 2023, *ACS Sustainable Chemistry & Engineering*, 11 (40), pp.14710-14722. 10.1021/acssuschemeng.3c02633 . hal-04288647

HAL Id: hal-04288647

<https://hal.univ-lille.fr/hal-04288647v1>

Submitted on 22 Dec 2023

HAL is a multi-disciplinary open access archive for the deposit and dissemination of scientific research documents, whether they are published or not. The documents may come from teaching and research institutions in France or abroad, or from public or private research centers.

L'archive ouverte pluridisciplinaire **HAL**, est destinée au dépôt et à la diffusion de documents scientifiques de niveau recherche, publiés ou non, émanant des établissements d'enseignement et de recherche français ou étrangers, des laboratoires publics ou privés.

Impact of acidity and metal particle size on the competitive pathways of benzylphenyl ether conversion to aromatics and cycloalkanes in a non-polar solvent

Raphaella Azevedo Rafael¹, Robert Wojcieszak¹, Eric Marceau¹, Fabio Bellot Noronha^{1,2*}

¹Univ. Lille, CNRS, Centrale Lille, Univ. Artois, UMR 8181 – UCCS – Unité de Catalyse et Chimie du Solide, F-59000 Lille, France.

²National Institute of Technology, Catalysis, Biocatalysis and Chemical Processes Division, Av. Venezuela 82, 20081-312, Rio de Janeiro, Brazil

* Corresponding author: fabio.bellot@int.gov.br

Submitted to

ACS Sustainable Chemistry & Engineering

Revised July 2023

Abstract

This work investigates the role of the support and metal particle size on the performance of Pd-based catalysts for the hydroconversion of benzyl phenyl ether (BPE) in the liquid phase. Pd-based catalysts supported on different oxides (SiO_2 , TiO_2 , Nb_2O_5 , Al_2O_3 , ZrO_2 , and HZSM5) were synthesized by incipient wetness impregnation (particle size > 4 nm) and sol-immobilization methods (particle size < 4 nm). Different reaction pathways leading to aromatics, polyaromatics or cycloalkanes have been evidenced, and the role of the support acidity and metal particle size on the competition between these pathways has been clarified. The acid sites of the support themselves promote the cracking of the $\text{C}_{\text{aliph}}\text{-O}$ bond of BPE, producing monoaromatic intermediates that react with each other to form polyaromatic dimers and trimers. Besides, the hydrogenolysis of the $\text{C}_{\text{aliph}}\text{-O}$ bond takes place on the metallic Pd particles, producing toluene and phenol, but polyaromatics are still formed in a parallel pathway when the catalysts present large Pd particles. In contrast, on catalysts containing small Pd particles, this competitive pathway is suppressed. Moreover, toluene and phenol are hydrogenated, and completely deoxygenated cycloalkanes are obtained. These results stress the importance of the balance between metal particle size and support acidity for the production of cycloalkanes from aryl ethers. Finally, a reaction network that takes simultaneously into account the characteristics of the metal (particle size) and of the support (acidity) is proposed.

Keywords: Benzyl phenyl ether; Hydrodeoxygenation; Hydrogenolysis; Pd-based catalysts; Metal particle size; acid sites.

Introduction

Lignocellulosic biomass is an abundant, non-edible, and renewable resource for the production of highvalue-added chemicals and fuels in future biorefineries ¹⁻⁴. Lignocellulosic biomass is composed mainly by cellulose (40-50%), hemicellulose (25-35%), and lignin (15-20%) ^{5,6}. Cellulose and hemicellulose are widely used for the production of bioethanol and other chemical products, whereas lignin has limited application due to its complex structure, which makes its depolymerization difficult ⁷. Currently, approximately 2% of industrial lignin is commercially used, while the rest is burnt for heat generation through combustion ⁸. However, there is an enormous potential market for value-added chemicals and fuels derived from lignin ⁹.

Different technologies are reported in the literature for the fractionation of the lignocellulosic biomass and for lignin depolymerization ¹⁰⁻¹². In these processes, lignin is converted into bio-oil, a mixture of several phenolic compounds, considered as a potential alternative source for the petroleum-based fuel and chemical industry ^{13,14}. However, due to its low calorific power, high acidity, and high content of oxygen, bio-oil is chemically and thermally unstable. In order to be used as a fuel for vehicles, it must be upgraded ¹⁵.

The hydrodeoxygenation (HDO) process is a promising technology for improving the quality of bio-oil. It aims at removing oxygen atoms to produce hydrocarbons, in presence of hydrogen and of a catalyst⁶. Due to the complexity and variety of molecules in bio-oil, model molecules representative of the different C-C and C-O bonds are commonly used for catalytic screening and elucidating mechanisms¹⁵. The main C-O and C-C bonds present in the lignin structure are the β -O-4, 4-O-5, α -O-4, 5-5, and β -5 linkages¹⁶. Among them, the α -O-4 linkage is the most reactive and the most thermally unstable one, because of the low bond dissociation energy of the aliphatic C-O bond¹⁷.

The conversion of benzyl phenyl ether (BPE), a typical model molecule representative of the α -O-4 ether linkage, has been studied in the literature^{8,13,14,17-25}. Quite different catalysts and reaction conditions have been used for the HDO of BPE, which makes any comparison challenging, and then, the reaction pathways involved in the cleavage of the α -O-4 bond and in the subsequent formation of products are still under debate. In particular, the formation of oxygen-bearing dimeric aromatic molecules, by rearrangement of the benzyl and phenyl moieties, has been observed in a few works^{14,17,20,24-26} but how the characteristics of the catalyst may affect this pathway with respect to the hydrogenolysis reaction is not clear yet. On the other hand, and quite surprisingly, the effect of the metal particle size on the cleavage of the α -O-4 bond and on subsequent reactions has not been studied at all, though it is expected to play a role in the hydrogenolysis or hydrogenation processes, at least via the number of surface metallic sites. From the results reported in the literature, some questions are still unanswered, and they will be addressed in our work. Does the type of acid sites (Lewis and Bronsted acid sites) affect the extent of the alkylation reaction pathway with respect to the pathways leading to monomeric species? Furthermore, are there any competitive pathways between the metal and acid sites that depends on the metal particle size? Is there an adequate balance between metallic sites (and the particle size) and acid sites necessary to promote complete deoxygenation of the BPE molecule and drive the reaction toward aromatics or cycloalkanes?

Therefore, this work aims at investigating the role of the support acidity and metal particle size on the reaction pathways involved in the hydroconversion of the BPE molecule, in the same conditions of temperature and pressure, and at identifying the catalyst characteristics favoring the production of O-containing polyaromatics, O-bearing or O-free aromatics, and O-bearing or O-free cycloalkanes. For this, Pd-based catalysts were prepared through two different methodologies

(incipient wetness impregnation and sol-immobilization method) in order to vary the metal particle size, and different oxides (SiO_2 , TiO_2 , Nb_2O_5 , Al_2O_3 , ZrO_2 , and HZSM5) were used as supports exhibiting various total acidity and acid sites (Lewis and Brønsted-type).

Experimental section

Preparation of Pd-based catalysts by incipient wetness impregnation method (imp)

SiO₂ (silica fumed, average particle size 0.2 – 0.3 μm, Sigma Aldrich, S5505), Al₂O₃ (Puralox NWA155), TiO₂ (P25, Sigma-Aldrich), Nb₂O₅ (CBMM), ZrO₂ (Saint Gobain), and HZSM5 (Zeolyst CBV 2314) were used to prepare the supported Pd catalysts by impregnation. Due to its low density, SiO₂ was moistened with deionized water and then, calcined in a muffle oven at 673 K (2 K min⁻¹) for 3 h. Nb₂O₅ was obtained by calcination of niobic acid (CBMM) in a muffle oven at 673 K (2 K min⁻¹) for 3 h. The Pd catalysts were prepared by incipient wetness impregnation using an aqueous solution of palladium (II) nitrate hydrate (Pd(NO₃)₂.xH₂O, Alfa Aesar). After impregnation, the samples were dried at 373 K for 12 h, then calcined at 673 K (2 K min⁻¹) for 3h in a muffle oven. The following catalysts were prepared: Pd/SiO₂-imp, Pd/Al₂O₃-imp, Pd/TiO₂-imp, Pd/Nb₂O₅-imp, Pd/ZrO₂-imp, and Pd/HZSM5-imp.

Preparation of Pd-based catalysts by sol-immobilization method (sol)

Al₂O₃ (Puralox NWA155), TiO₂ (P25, Sigma-Aldrich), Nb₂O₅ (CBMM), and ZrO₂ (Saint Gobain) were used to prepare the supported Pd catalysts by the sol-immobilization method. Nb₂O₅ was obtained as described above. 0.094 mmol of K₂PdCl₄ (Sigma-Aldrich) and 0.7 mL of a 2% solution of poly(vinyl alcohol) (Sigma-Aldrich, Mw: 9.000-10.000, 80% hydrolyzed) were added to 800 mL of deionized water, and the suspension was magnetically stirred for 10 min. Then, 4.7 mL of a 0.1M NaBH₄ solution (Sigma-Aldrich) was added into the flask dropwise. After 30 min, 990 mg of support was added and the pH was corrected to 2 by the addition of H₂SO₄. The mixture was stirred for 2 h. Finally, the catalyst was filtered, washed with 400 mL of deionized water, and

dried in a muffle oven at 373 K for 3 h. The catalysts synthesized were designated as Pd/Al₂O₃-sol, Pd/TiO₂-sol, Pd/Nb₂O₅-sol, and Pd/ZrO₂-sol.

Catalyst characterization

The Pd content of each sample was determined by inductively coupled plasma-optic emission spectroscopy (720-ES ICP-OES, Agilent) with axially viewing and simultaneous CCD detection. The samples (10 mg) were digested with a solution containing 250 μL of HF, 500 μl of H₂SO₄, and 4 mL of aqua regia (1HNO₃ + 3HCl) and heated at 383 K for 2 h in the autodigestor Vulcan 42 (Questron). The specific surface area of the samples was measured on a Micromeritics ASAP 2020 analyzer by N₂ physisorption, at the boiling temperature of nitrogen. The X-ray powder diffraction (XRD) patterns were obtained using a BRUKER D8 Advancer diffractometer with Cu K_α radiation ($\lambda = 0.1542$ nm) over a 2θ range of 10-70° at a scan rate of 0.02 °/step and a scan time of 1 s/step. The crystalline phases were identified by comparing the experimental diffractograms and the diffraction standards available from the Joint Committee on Powder Diffraction Standards – International Center for Diffraction Data (JCPDS - ICDD). When possible, the crystallite size of the particles was estimated by the Scherrer equation, described in Eq. 1, where K is a dimensionless shape factor, with a typical value of 0.9, λ is the X-ray wavelength (0.1542 nm), β is the full width at half maximum (FWHM) of the selected peak, and θ is the Bragg angle.

$$d = \frac{K\lambda}{\beta \cos\theta} \quad (\text{Eq. 1})$$

The Pd particle size distribution was measured by scanning transmission electron microscopy (STEM). Before STEM analyses, the impregnated catalysts were reduced (673 K under

30 bar of H₂), and then passivated at room temperature under 5% O₂/N₂ (30 mL/min) for 2 h. The metal catalysts were dispersed in isopropanol by ultrasonication and the suspensions were dropped on holey carbon-coated copper grids. At least 200 particles were taken into account for the determination of the particle size distribution. The images were obtained using a MET FEI Titan X-FEG with a voltage of 300 kV equipped with a high-angle annular bright field and dark-field detector (HAADF), which can provide images with Z-contrast with a resolution of 0.7 Å.

In addition, these data enabled the calculation of metal dispersion (D) by considering the mean diameter of the metal particles (dp) based on equations 2 and 3:

$$dp = \frac{\sum ni di}{\sum ni} \quad (\text{Eq. 2})$$

$$D = 6 \frac{Vm/am}{dp} \quad (\text{Eq. 3})$$

where *ni* is the number of spherical particles of diameter *di*, *Vm* is the volume of the metal atom, and *am* is the surface area occupied by an atom. The volume of metal is described in equation 4:

$$Vm = \frac{M}{\rho NA} \quad (\text{Eq. 4})$$

where *M* is the atomic mass, ρ the mass density and *NA* is the Avogadro number (6.022 × 10²³ mol⁻¹). In the case of palladium: *M* = 106.4 g mol⁻¹; ρ = 12.02 g cm⁻³; *Vm* = 14.70 Å³ and *am* = 7.93 Å². Replacing *Vm* and *am* values on equation 3 gives the following relationship between metal dispersion and the mean particle diameter (nm) equation 5:

$$D (\%) = \frac{1.1093}{dp} \times 100 \quad (\text{Eq. 5})$$

The concentration of acid sites was measured by temperature-programmed desorption of ammonia (NH₃-TPD) in an AutoChem II equipment from Micromeritics, equipped with a thermal conductivity detector and a mass spectrometer. The catalysts prepared by incipient wetness impregnation (100 mg) were previously reduced under a flow of 40 mL min⁻¹ in pure H₂ (heating of 10 K min⁻¹ to 673K, for 1 h), and then purged in a He flow (30 mL min⁻¹) for 30 min. After reduction, the samples were cooled to 373 K, and the gas was switched to a mixture containing 10% of NH₃ in He (30 mL min⁻¹) for 30 min. The physisorbed ammonia was flushed out with He (50 mL min⁻¹) for 2 h. Then, the catalysts were heated under He at 10 K min⁻¹ to 773 K. The catalysts synthesized by the sol immobilization method followed the same procedure described above but without the reduction step. The nature and concentration of acid sites were measured by pyridine adsorption experiments followed by Fourier-Transform Infrared Spectroscopy (FTIR). The analyses were performed using a Thermo Nicolet Protege 460 instrument equipped with a CsI beam splitter and a MCT detector with a 2 cm⁻¹ resolution. Before analysis, the calcined samples were pressed (1 ton cm⁻²) into a self-supported wafer (2.01 cm²), placed in a quartz sample holder, and then in a quartz cell equipped with KBr windows. Catalysts samples were treated under high vacuum ($P < 10^{-7}$ mbar) at 723 K overnight. Pyridine was then adsorbed at 373 K and the samples were evacuated at 423 K under high vacuum ($P < 10^{-7}$ mbar) for 30 min between spectra acquisition. The bands located at 1452 and 1543 cm⁻¹ were used for the quantification of the coordinated pyridine to Lewis ($\epsilon_L = 2.22 \text{ cm } \mu\text{mol}^{-1}$) and Brønsted ($\epsilon_B = 1.67 \text{ cm } \mu\text{mol}^{-1}$) sites respectively

Catalytic activity

The conversion of benzyl phenyl ether (BPE) was carried out in a 50 mL autoclave Parr reactor equipped with a magnetic stirrer. Before the catalytic test, the impregnated catalysts were previously reduced under 30 bar H₂ (50 ml min⁻¹) at 673 K for 1 h in the Screening Pressure Reactor (SPR). After reduction, all catalysts were stored inside a glove box. In a typical test with impregnated catalysts, the reactor was loaded inside the glove box with the desired quantity of catalyst (25 – 250 mg) and 15 mL of reaction mixture containing benzyl phenyl ether in decalin (62 mmol). For the catalysts prepared by the sol-immobilization method, the catalyst was loaded directly into the reactor without a glove box or reduction treatment using the same concentration of BPE. After loading, the vessel was connected to the unit, purged 3 times with hydrogen, and pressurized with 18 bar of H₂. The reaction mixture was heated up to 503 K (5 K min⁻¹) and then stirred (600 rpm) for 3 h. In the end, the reactor was cooled in an ice bath below 313 K, and the liquid samples were filtered and analyzed by GC-FID (Agilent Technologies 5977B MSD), equipped with a CP-Wax 52 CB column (polyethylene glycol phase, 30 m x 250 μm, 0.250 μm). The chromatographic method had a flow rate of 1.7 mL/min of N₂ as the carrier gas, 1: 100 split ratio, injector temperature of 523 K, and the temperature program based on five steps: isothermal at 313 K for 3.5 min; ramp up to 423 K at 15 K min⁻¹ for 1 min, ramp up to 468 K at 25 K min⁻¹ for 2 min, then ramp up 478 K at 2 K min⁻¹ for 1 min and ramp up 523 K at 20 K min⁻¹ for 10 min.

The identification of the products was carried out by gas chromatography coupled to mass spectrometry GC-MS (Agilent Technologies 5977B MSD) using the same column and conditions. The product conversion, yield, and mass balance for each product were calculated as follows:

$$X_{\text{BPE}} (\%) = \frac{(\text{Mass of subst.})_0 - (\text{Mass of subst.})_t}{(\text{Mass of subst.})_0} \times 100 \quad (\text{Eq. 6})$$

$$\text{Yield (\%)} = \frac{\text{Mass of product}}{\text{(Mass of subst.)}} \times 100 \quad (\text{Eq. 7})$$

$$\text{MB (\%)} = \Sigma \text{yield} + \frac{\text{(Mass of subst.)}_t}{\text{(Mass of subst.)}_0} \quad (\text{Eq. 8})$$

Where 0 corresponds to the beginning of the reaction and t at 3 h of reaction.

Results and Discussion

Catalyst Characterization

Table 1 summarizes the chemical composition and the specific surface area of the supported catalysts. The Pd contents for the catalysts prepared by incipient wetness impregnation were around 1.8 – 2.0 wt.% whereas for the ones prepared by sol immobilization varied from 0.3 to 0.9 wt.%. There was no sodium residue after catalyst preparation by sol immobilization method. Pd/SiO₂-imp and Pd/HZSM5-imp exhibited the largest specific surface area (182 and 393 m² g⁻¹, respectively), while the smallest ones were observed for Pd/TiO₂-imp and Pd/Nb₂O₅-imp (45 and 65 m² g⁻¹, respectively).

The N₂ adsorption-desorption isotherms for all supported catalysts are presented in Figs S1-S6 (supplementary information). All samples display a type IV isotherm, except for Pd/HZSM5 which exhibit a type I isotherm characteristic of microporous materials. For those who present a type IV isotherm, typical for mesoporous solids, a hysteresis loop of type H1 is observed for Pd/SiO₂-imp, Pd/TiO₂-imp, Pd/TiO₂-sol, and Pd/ZrO₂-imp, while for the other materials a hysteresis loop of type H3 is observed. In addition, for Pd/ZrO₂-sol, a second step in the isotherm at P/P₀ = 0.8 indicates the presence of multi pore distribution²⁷.

Table 1. Pd content, specific area (S_{BET}), pore volume (PV), metal particle size (d_p), and metal dispersion (D) of palladium supported catalysts.

Catalysts	Pd wt% ^a	S_{BET} ($\text{m}^2 \text{g}^{-1}$)	PV ($\text{cm}^3 \text{g}^{-1}$)	d_p (nm) ^c	D (%) ^e
Pd/SiO ₂ -imp	1.8	182 (189) ^b	0.90	7.2 (17) ^d	14
Pd/Al ₂ O ₃ -imp	1.7	148 (151)	0.40	24.5	4
Pd/TiO ₂ -imp	2.0	45 (45)	0.23	9.0	11
Pd/Nb ₂ O ₅ -imp	1.9	65 (105)	0.11	6.8 (9)	15
Pd/ZrO ₂ -imp	1.8	136 (141)	0.22	13.1	8
Pd/HZSM5-imp	1.8	393 (485)	0.39	24.6 (22)	4
Pd/Al ₂ O ₃ -sol	0.4	158 (151)	0.40	3.8	26
Pd/TiO ₂ -sol	0.9	56 (45)	0.22	3.4	29
Pd/Nb ₂ O ₅ -sol	0.9	99 (105)	0.11	2.0	50
Pd/ZrO ₂ -sol	0.3	154 (141)	0.18	2.7	37

^a Measured by ICP; ^bIn brackets, specific surface area of the bare support; ^c Average particle size measured by TEM; ^d Crystallite diameter estimated by XRD through Scherrer equation; ^e Pd dispersion calculated by $D=1.1093/d_p$.

X-ray diffraction patterns for the supports and impregnated and sol-immobilized catalysts reduced at 673 K under 30 bar of H₂ are shown in Fig. 1. The diffractogram of SiO₂ exhibited a broad diffraction peak at $2\theta = 20^\circ$ corresponding to non-crystalline SiO₂. The diffractogram of Al₂O₃ exhibited the lines from γ -Al₂O₃ (PDF: 00-001-1310). For TiO₂, the characteristic lines corresponding to the anatase (PDF: 01-073-1764) and rutile (PDF: 01-089-8303) phases of titania were observed. Nb₂O₅ also appeared as a poorly crystalline phase; the absence of a diffraction pattern is consistent with the calcination temperature, as reported in the literature^{28,29}. The typical

lines from tetragonal ZrO₂ (PDF: 00-050-1089), and from monoclinic ZrO₂ (PDF: 04-002-8305), were observed for zirconia. Finally, HZSM5 exhibited the characteristic diffraction lines from the MFI zeolitic structure (PDF: 00-057-0145). Concerning the reduced Pd-based catalysts, the diffractograms were close to those from the supports. The characteristic lines of metallic Pd at $2\theta = 40.02^\circ$ and 46.49° (PDF: 01-087-0638) could be observed only for some of the impregnated catalysts (Pd/SiO₂-imp, Pd/Nb₂O₅-imp, and Pd/HZSM5-imp) and are hidden by the diffraction lines of the support in the other cases. When possible, the average crystallite size was calculated via the Scherrer equation using the Pd⁰ (111) line at $2\theta = 40.02^\circ$, and the results are reported in Table 1. The largest crystallite size (22.0 nm) was observed for Pd/HZSM5-imp and the smallest one for Pd/Nb₂O₅-imp (9.0 nm). For the sol-immobilized catalysts, the diffraction lines from metallic Pd were not detected, which is likely due to the small metal particle size obtained in these catalysts or to the low metal content.

STEM images of Pd/Nb₂O₅-imp and Pd/Nb₂O₅-sol and their respective particle size distribution are shown in Fig. 2. The STEM images and the particle size distribution for the other impregnated and sol-immobilized catalysts are presented in Figs. S7 – S14 (Supplementary information).

For all catalysts, the palladium particles had a spherical, or close to spherical, shape. In general, all materials showed a good contrast, and the palladium particles were easily distinguished from the support. However, for the zirconia-supported catalysts, the contrast was poor and it was difficult to distinguish the Pd particles on the images. Therefore, it was not possible to establish the size distribution, and the Pd particle size was only estimated by counting a few visible Pd particles for Pd/ZrO₂-sol.

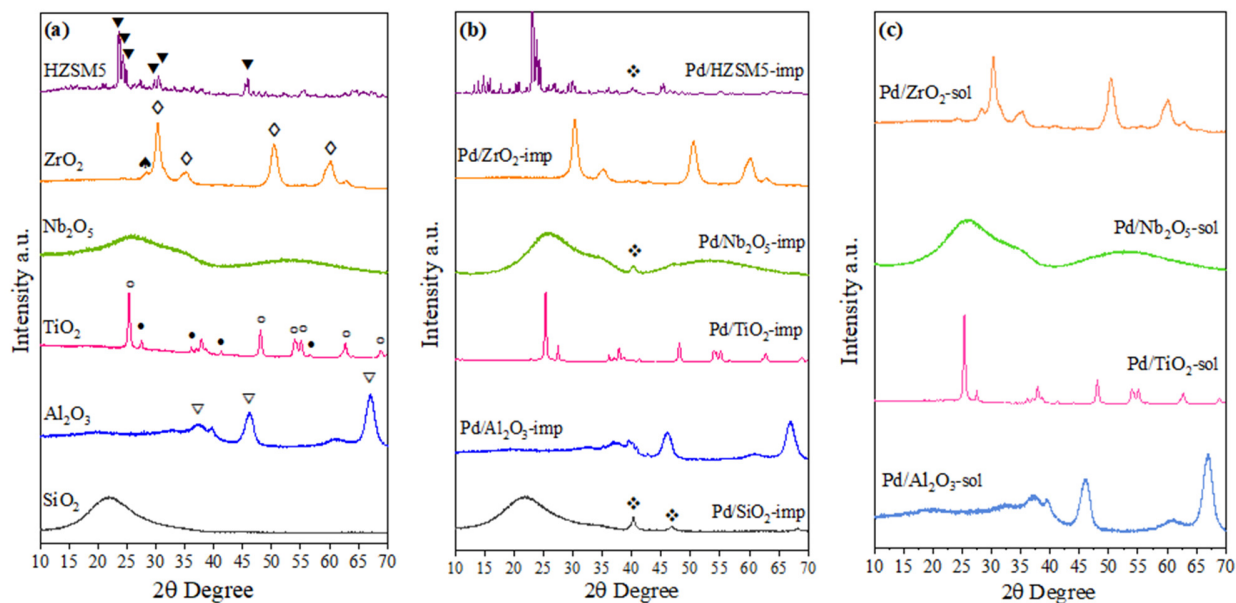


Figure 1- Diffractograms of (a) supports and Pd-based catalysts: (b) impregnated catalysts; (c) sol-immobilized catalysts. (▼) HZSM5; (◆) tetragonal ZrO₂; (♠) monoclinic ZrO₂; (▽) γ -Al₂O₃; (○) Anatase TiO₂; (●) Rutile TiO₂; (▽) γ -Al₂O₃; (♦) Pd⁰.

In case of the impregnated catalysts, TEM images showed that the Pd particles are quite different in size. Among them, Pd/Al₂O₃-imp and Pd/HZSM5-imp exhibited the largest average particle size (24 nm), while Pd/SiO₂-imp and Pd/Nb₂O₅-imp showed the smallest one (7.2 and 6.8 nm, respectively), (Table 1). This result is in accordance with the crystallite size estimated by the Scherrer equation. Compared to the impregnated catalysts, the sol-immobilized catalysts exhibited smaller Pd particle size. For these catalysts, the Pd particles exhibited a narrow size distribution and the images show that Pd particles are well dispersed over the support. For instance, the average Pd particle size of Pd/Nb₂O₅-imp and Pd/Nb₂O₅-sol catalysts were 6.8 and 2.0 nm, respectively (Fig. 2 b and d). Despite the large Pd particles observed by TEM for Pd/Al₂O₃-imp, the lines of metallic Pd were not detected by XRD probably because these lines are overlapping with the diffraction lines of the support.

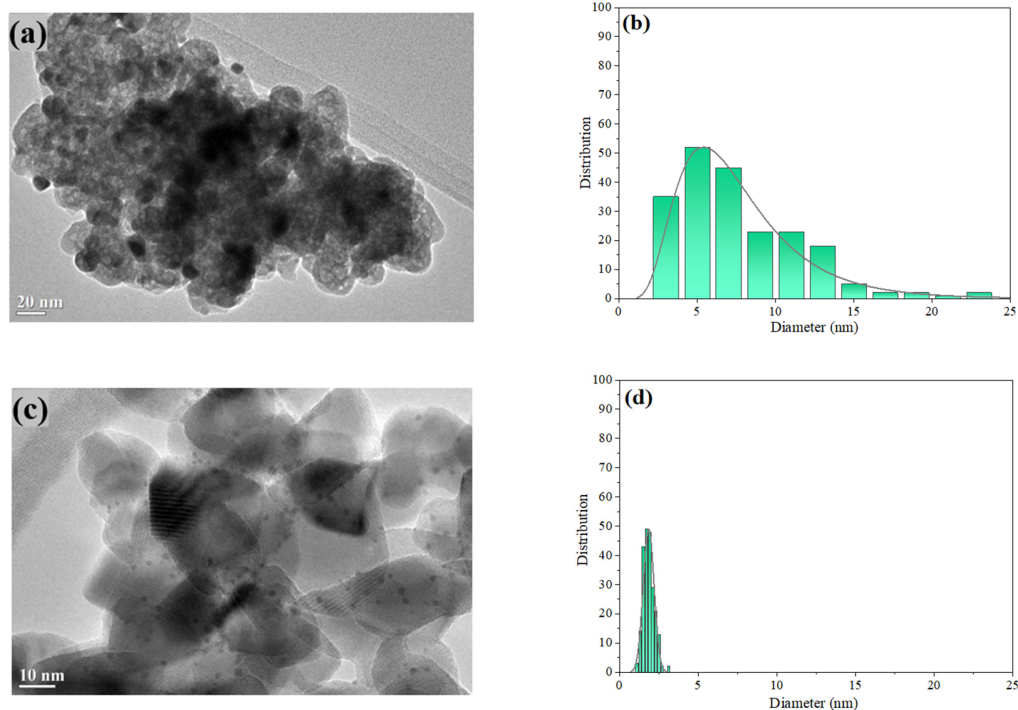


Figure 2 - STEM images and particle size distribution of (a and b) Pd/Nb₂O₅-imp and (c and d) Pd/Nb₂O₅-sol.

From the STEM results, the metal dispersion was calculated considering equation 5. The metal dispersion varied between 5 to 51% depending on the support and the preparation method (Table 1).

The acid properties of the catalysts were first assessed by NH₃-TPD, whose profiles are shown in Fig. 3. All catalysts exhibited multiple and poorly resolved peaks between 373 and 773 K, indicating the presence of acid sites with different strengths. The relative contribution of each desorption peak was obtained by deconvolution of the TPD profiles, considering the adsorption of NH₃ on three different groups of acid sites (weak: T < 523 K; medium: 523 < T < 593 K; strong: T > 593 K). The experimental data were fitted using a multiple-Gaussian function.

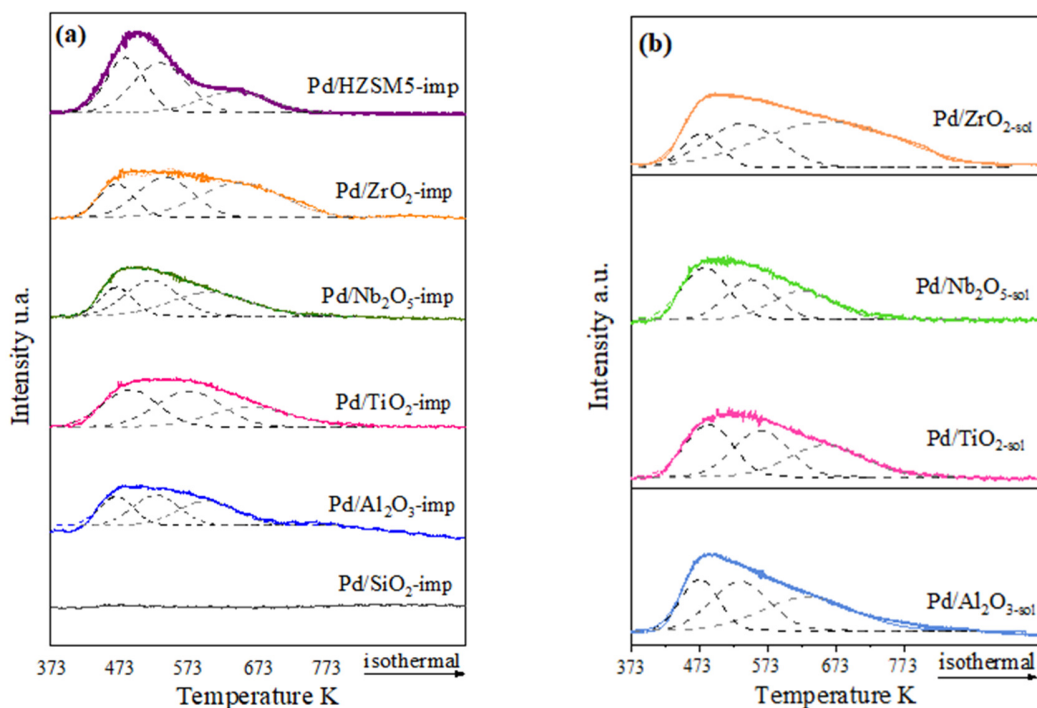


Figure 3- NH₃-TPD profiles for supported Pd-based catalysts: (a) impregnated catalysts, (b) sol-immobilized catalysts.

Table 2 reports the total amount of acid sites as well as their strength distribution. Concerning the impregnated catalysts, Pd/SiO₂-imp did not retain NH₃. Pd supported over HZSM5-imp exhibited the highest concentration of acid sites (699 μmol NH₃g⁻¹), and the order was: Pd/HZSM5-imp >> Pd/ZrO₂-imp > Pd/Nb₂O₅-imp ≈ Pd/TiO₂-imp ≈ Pd/Al₂O₃-imp.

The sol-immobilized catalysts exhibited a higher concentration of acid sites compared to the respective impregnated catalysts, probably because, unlike impregnated catalysts, these catalysts did not undergo any heat treatment to complete their preparation. In contrast, the impregnated catalysts were calcined at 673 K after impregnation and reduced under H₂ at 673 K before NH₃ adsorption, which may decrease their total concentration of acid sites. However, the surface area of the catalysts prepared by sol-immobilization was also higher and thus, the density

of acid sites was approximately the same for Pd supported on Nb₂O₅ and TiO₂ synthesized by both methods.

The distribution of Lewis and Brønsted acid sites was evaluated by FTIR of adsorbed pyridine. Fig. 4 shows the spectra of pyridine adsorbed on Pd-based catalysts after outgassing at 423 K, on catalysts pretreated at 723 K. The band at 1545 cm⁻¹ represents the pyridine chemisorbed on the Brønsted acid sites (BAS), while the band at 1445 cm⁻¹ is attributed to the pyridine coordinated to the Lewis acid sites (LAS). Pd/Al₂O₃-imp and Pd/TiO₂-imp exhibited only LAS, while Pd/Nb₂O₅-imp, Pd/ZrO₂-imp, and Pd/HZSM5-imp also showed BAS. The same result was observed for the sol-immobilized catalysts. The fraction of BAS and LAS measured through the areas of the bands at 1545 and 1445 cm⁻¹, respectively, are reported in Table 2. For the impregnated catalysts, Pd/HZSM5-imp exhibited the highest fraction of BAS, following the order: Pd/HZSM5-imp > Pd/ZrO₂-imp > Pd/Nb₂O₅-imp. Regarding the sol-immobilized catalysts, the highest fraction of BAS was observed for Pd/Nb₂O₅-sol.

Table 2- Total amount of ammonia desorbed, acid sites strength distribution, and concentration of Lewis and Brønsted acid sites for palladium-based catalysts.

Catalysts	NH ₃ desorbed ($\mu\text{mol g}^{-1}$) ^a	Acid sites strength distribution (%) ^a			Distribution (%)	
		Weak	Medium	Strong	LAS ^b	BAS ^b
Pd/SiO ₂ -imp	0	0	0	0	0	0
Pd/Al ₂ O ₃ -imp	160	26	35	35	100	0
Pd/TiO ₂ -imp	169	35	40	27	100	0
Pd/Nb ₂ O ₅ -imp	167	31	27	42	82	18
Pd/ZrO ₂ -imp	251	19	35	46	70	30
Pd/HZSM5-imp	699	34	42	24	40	60
Pd/Al ₂ O ₃ -sol	301	24	36	39	100	0
Pd/TiO ₂ -sol	231	31	32	29	100	0
Pd/Nb ₂ O ₅ -sol	259	39	31	28	79	21
Pd/ZrO ₂ -sol	479	12	29	59	93	7

^a Determined by NH₃-TPD; ^b Determined by pyridine adsorption-FTIR after outgassing at 423 K. LAS: Concentration of Lewis acid sites, BAS: Concentration of Brønsted acid sites ($\mu\text{mol g}^{-1}$)

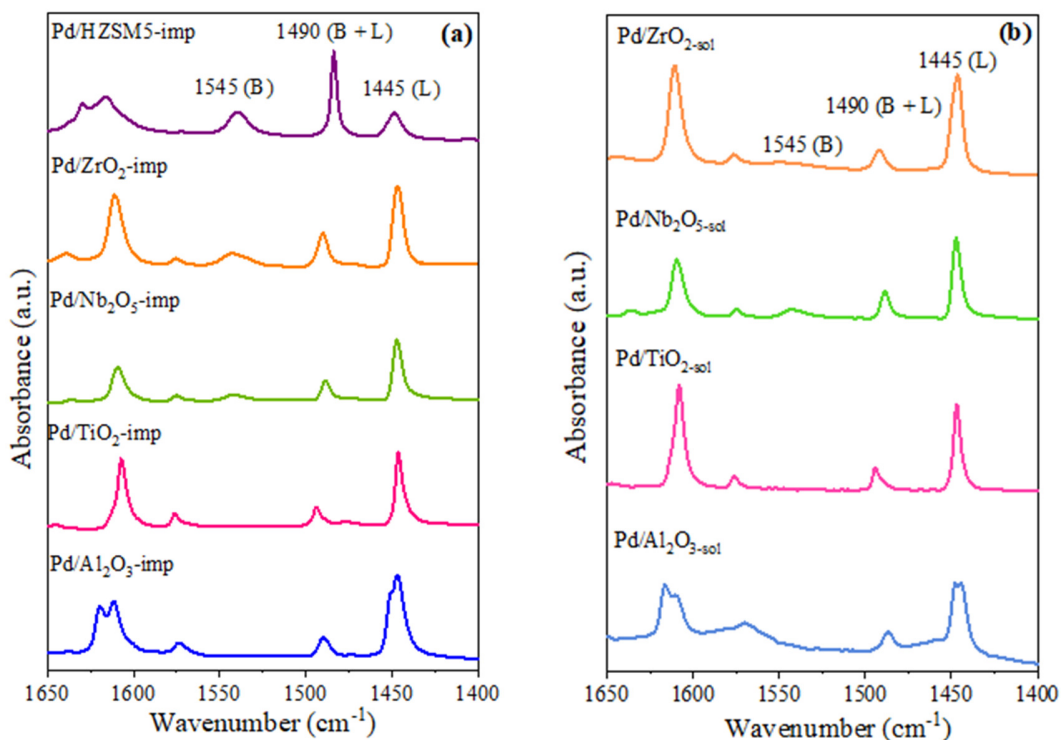


Figure 4- Infrared spectrum of adsorbed pyridine on Pd-based catalysts at 423 K. (a) impregnated catalysts, (b) sol-immobilized catalysts.

Conversion of benzyl phenyl ether

Activity of bare supports and correlation with their acidity

The product distribution for the conversion of BPE for 3 h over the bare supports at 503 K, under 18 bar of H₂ in decalin, is presented in Table 3. In the absence of support, no conversion of BPE was observed. When an oxide was introduced, BPE was converted to a minor or large extent, except for SiO₂. This oxide did not exhibit any activity even using a four-fold larger mass compared to the other oxides. This is likely due to its total absence of acidity (Table 3, entry 1). Using the same mass of solid (60 mg), Al₂O₃ and TiO₂ showed the lowest BPE conversion while Nb₂O₅ and ZrO₂ presented the highest one (Table 3, entries 2-5). Regarding the product distribution, aromatic

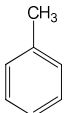
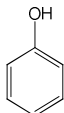
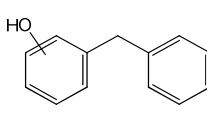
dimers 2-benzylphenol and 4-benzylphenol (2-BPH and 4-BPH, called alkylated products), and to a lesser extent, phenol, were the main products formed. Toluene always appeared as a minor product. In addition, an aromatic trimer (2,6-dibenzylphenol) was also detected in a significant amount over ZrO_2 and especially Nb_2O_5 . The yield of dimers and trimers followed the order: $Nb_2O_5 > ZrO_2 > HZSM5 \gg TiO_2 \approx Al_2O_3$. In the absence of a metallic site, an oxide with Brønsted acid sites, exhibits higher activity and selectivity to alkylated products, compared with oxides with only Lewis acid sites such as alumina and titania. Therefore, the cleavage of the ether linkage can thus take place in the absence of a metallic phase.

The formation of alkylated products has been reported in polar^{17,20,24,25} or non-polar¹⁷ solvents. In a non-polar solvent, as has been chosen in our work, whether in the absence of a catalyst or in the presence of a non-acid support like silica, a high selectivity to alkylated products such as 4-BPH and 2-BPH (above 90%) has been reported^{17,25,26}. It has been proposed that under these conditions, the cleavage of the $C_{aliph}-O$ bond of BPE proceeds through pyrolysis reaction, and the alkylated products were formed through reactions between the resulting phenoxy and benzyl radicals. According to Robert et al.²⁵, toluene and phenol would also be produced when these radicals could combine with hydrogen. The formation of alkylated products at low temperatures (< 523 K) has also been reported when an acid support like silica-alumina was used¹⁴. In this case, it was proposed that the alkylated products were produced through a Claisen rearrangement³⁰. According to the authors, the formation of alkylated products was promoted by the H_2 -deficient environment, since silica-alumina does not adsorb and activate hydrogen. Trimers would be formed by the reaction between one phenol molecule with two toluene molecules, which explains the depletion of toluene with respect to phenol. He et al.³¹ proposed that the protons from Brønsted acid sites of zeolites are donated to the oxygen atom of BPE and merely activate the bond. The weakened

C-O bond is broken, producing radicals leading to the formation of alkylated products, or of toluene and phenol if H radicals are also present. In contrast, Katritzky et al.³² reported that the heterolytic cleavage of the BPE ether bond produces a benzyl cation, which reacts with phenol to form 2 and 4-BPE. However, for the conversion of BPE in undecane, DFT calculations showed that the alkylated products were formed through free-radical reactions via pyrolysis, instead of carbocation formation, due to the lower bond dissociation energy required to form phenoxy and benzyl radicals compared to benzyl cation and phenoxy anion (184.3 and 627.7 kJ mol⁻¹, respectively)¹⁷.

Therefore, the BPE conversion into aromatic dimers (2-BPH and 4-BPH) and trimers probably proceeds in our work through the free-radical reactions described in the literature. The important conclusion is that this reaction is more general than reported so far, and appears to be catalyzed by the acid sites of a wider range of oxides, following the order: non-acid supports (inactive) < supports with Lewis acid sites < supports with Brønsted acid sites. Concerning the trimer formation, 2,6-dibenzylphenol was only formed over Nb₂O₅ and ZrO₂. Despite the high acidity of HZSM5, the trimer formation did not occur, which is likely due to steric hindrance caused by the small pore diameter of the zeolite channels. The coupling between a large molecule (2-BPH) with a second benzyl radical is consequently suppressed.

Table 3- Conversion of benzyl phenyl ether (X_{BPE}), mass balance (MB), and product distribution for supports and impregnated catalysts (503 K, 18 bar of H_2 in decalin, 3h).

Entry	Catalyst	X_{BPE} (%)	MB (%)	Yield (%)			Trimer
							
1	SiO_2	0.0	--	0.0	0.0	0.0	0.0
2	Al_2O_3	7	98	0.1	2.7	1.6	0.0
3	TiO_2	9	98	1.4	2.1	3.5	0.0
4	Nb_2O_5	100	89	0.0	15.0	45.0	29.3
5	ZrO_2	100	71	1.0	16.0	48.0	9.4
6	HZSM5	29	95	0.2	4.9	19.1	0.0
7	Pd/ SiO_2 -imp	41	90	18.2	13.0	0.0	0.0
8	Pd/ Al_2O_3 -imp	60	94	23.3	22.1	8.3	0.0
9	Pd/ TiO_2 -imp	52	100	24.8	23.9	4.7	0.0
10	Pd/ Nb_2O_5 -imp	58	91	21.5	20.0	8.2	0.0
11	Pd/ ZrO_2 -imp	65	85	11.4	13.4	25.4	0.0
12	Pd/HZSM5-imp	59	91	4.7	10.9	33.6	0.0
13	Pd/ Nb_2O_5 -imp*	100	95	13.6	22.2	38.7	20.8

Reaction conditions: Reactant (62 mmol), decalin (15 mL), SiO_2 (250 mg), Al_2O_3 (60 mg) TiO_2 (70 mg), Nb_2O_5 (60 mg) ZrO_2 (60 mg), HZSM5 (60 mg), Pd/ SiO_2 -imp (250 mg), Pd/ Al_2O_3 -imp (25 mg) Pd/ TiO_2 -imp (130 mg), Pd/ Nb_2O_5 -imp (30 mg), Pd/ ZrO_2 -imp (65 mg), Pd/HZSM5-imp (45 mg), 503 K, 18 bar of H_2 , 3h. *Reaction performed with 60 mg of Pd/ Nb_2O_5 -imp to achieve complete BPE conversion

Competitive pathways between Pd and acid sites

The product distribution for the conversion of BPE over impregnated Pd-based catalysts, at 503 K, under 18 bar of H₂ in decalin, after 3 h, is reported in the lower part of Table 3 (conversion range: 52-65%, except for Pd/SiO₂-imp). In contrast with the bare supports, phenol and toluene were formed over all catalysts, even in the absence of acidity as observed for Pd/SiO₂-imp catalyst. This result suggests that metallic particles are active sites for the hydrogenolysis of the C_{aliph}-O bond of BPE (which agrees very well with the literature^{8,13,18,21,33}), but the hydrogenation of toluene and phenol is not performed under these reaction conditions on the impregnated catalysts.

Aromatic dimers (2-BPH and 4-BPH) were not produced over Pd/SiO₂-imp whereas they were formed for Pd/Al₂O₃-imp, Pd/TiO₂-imp, and Pd/Nb₂O₅-imp catalysts, indicating a competition between the hydrogenolysis of BPE on the Pd particles, and the participation of the acid sites of the support in the cleavage of the C_{aliph}-O bond of BPE. Indeed, for Pd/ZrO₂-imp and Pd/HZSM5-imp catalysts, alkylated products were mainly formed, which is likely due to the presence of Brønsted sites on these catalysts. The formation of alkylated products has also been reported in the literature for the conversion of BPE over metal supported on acid supports such as HZSM5^{17,33} and beta zeolites^{23,24}.

Increasing the BPE conversion confirms the prominence of the “acid sites” pathway leading to the production of alkylated products. Fig. 5 shows the product distribution as a function of BPE conversion over Pd/HZSM5-imp at 503 K, under 18 bar of H₂ in decalin. The increase of conversion was obtained by increasing the amount of catalyst. When the conversion was increased from 39 to 82 %, the yield of alkylated products linearly increased while the yields to phenol and toluene only slightly increased. For instance, the yields of 2-BPH increased from 10 % (X_{BPE} = 39 %) to 38 % (X_{BPE} = 82%). In addition, 2-BPH was the main alkylated product, with a lesser

formation of 4-BPH in the whole range of conversion. This result indicates that the attack of the benzyl radical onto the ortho position of phenol was preferential for all conversions. The preferential formation of 2-BPH was also observed by Yoon et al¹⁴ over silica-alumina. The same trend was observed for the Pd/Nb₂O₅-imp catalyst (Table 3, entry 13). At higher conversion, the yield to toluene decreased and the yield to dimers increased. In addition, trimers were now formed.

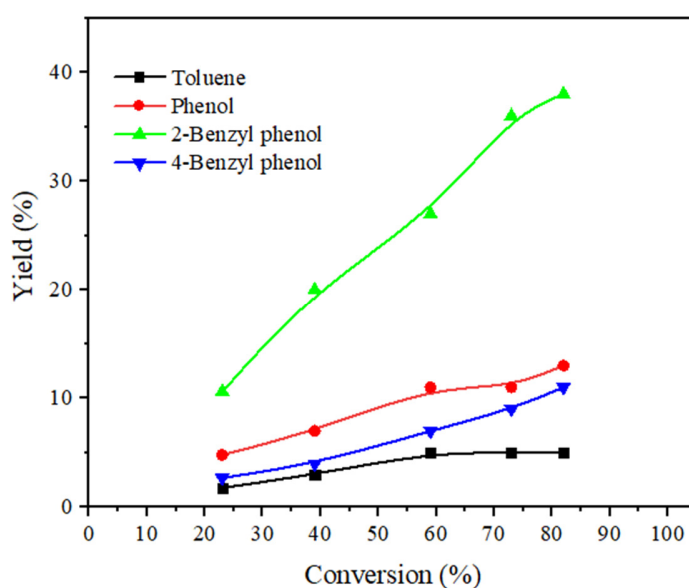


Figure 5- Yields of products as a function of BPE conversion. Reaction condition: 62 mmol BPE, Pd/HZSM5 (15 – 75 mg), 503 K, 18 bar of H₂ in decalin, 3h.

Based on the literature, it can be proposed that the mechanism for the cleavage of the C_{aliph}-O bond by the acid sites of the supports involves the formation of radicals, that may lead to phenol and toluene by reaction with H radicals. The formation of dimers on the supported Pd-based catalysts prepared by impregnation indicates that the metal sites are not able to transfer enough activated hydrogen to the support in order to terminate free-radical reactions initiated on it and to

undercut the dimers formation pathway. This can be due to the low metal-support interface at the periphery of the large Pd particles present on the impregnated catalysts (Table 1).

The influence of particle size

In order to study the influence of the Pd particle size on the competition between the reaction pathways, a sol-immobilization method was used to synthesize Pd-based catalysts with small metal particles (< 4 nm). Reduced metal nanoparticles are formed by the addition of a reducing agent, sodium borohydride, and then deposited onto the support³⁴⁻³⁶.

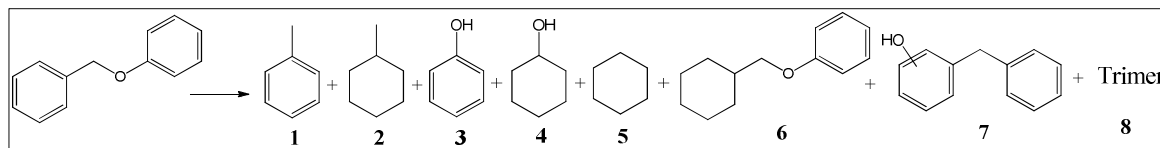
The catalysts prepared by the sol immobilization method were more active than the impregnated ones. For Pd/Al₂O₃-sol and Pd/TiO₂-sol, methylcyclohexane and cyclohexanol were the main products formed. Cyclohexane was also produced for Pd/Nb₂O₅-sol and Pd/ZrO₂-sol, two catalysts that possess Brønstedacid sites (Table 4, entries 1 - 4). Unlike impregnated catalysts, phenol and toluene were not observed, suggesting that both were rapidly hydrogenated to cyclohexanol and methylcyclohexane, respectively, regardless of the support.

Furthermore, the partial hydrogenation of BPE was also observed in some cases. This confirms that the small Pd particles are active in the hydrogenation of aromatic rings, which to some extent becomes a competing pathway with respect to the hydrogenolysis of BPE. Furthermore, alkylated products (2-BPH, 4-BPH, and 2,6-dibenzylphenol) were not detected despite the presence of Brønstedacid sites on some of the catalysts.

In order to evaluate the effect of Pd particle size on the conversion of BPE, we should compare the performance of Pd-based catalysts supported on the same oxide with approximately the same acid properties. This is the case for Pd/Nb₂O₅-imp and Pd/Nb₂O₅-sol catalysts that exhibits the same density of acid sites determined by NH₃-TPD (2.6 μmol m²) as well as similar distribution

of acid sites (18 and 21% Bronsted acid sites, respectively). The only difference between both catalysts was the Pd particle size: Pd/Nb₂O₅-imp has larger Pd particle size than Pd/Nb₂O₅-sol (6.8 and 2.0 nm). The product distribution of Pd/Nb₂O₅-imp and Pd/Nb₂O₅-sol catalysts was compared at the same high BPE conversion (Table 3, entry 13 and Table 4, entry 3, respectively). The main products formed over Pd/Nb₂O₅-sol was methylcyclohexane (45.9%) and cyclohexane (23.6%), whereas phenol (22.2%) and oligomers (59.5 %) were mainly produced over Pd/Nb₂O₅-imp. The yield to dimers was high (38.7%) and even trimers were formed (20.8%) for Pd/Nb₂O₅-imp. This reaction did not occur over the catalyst synthesized by the sol immobilization method. The same trend is observed for Pd/TiO₂-imp and Pd/TiO₂-sol catalysts, whose supports also show similar acid properties along with different Pd particle sizes. Therefore, the large Pd particles on the impregnated catalysts favored the BPE hydrogenolysis, but the subsequent hydrogenation of the hydrogenolysis products by metal particles and dehydration of cyclohexanol catalyzed by the support acid sites did not occur as observed for colloidal catalysts. For the impregnated catalysts, after BPE hydrogenolysis, the acid sites lead to the formation of alkylated products.

Table 4- Conversion of benzyl phenyl ether (X_{BPE}), mass balance (MB), and product distribution for supports and impregnated catalysts (503 K, 18 bar of H_2 in decalin, 3h).



Ent.	Catalyst	X_{BPE} (%)	MB (%)	Yield (%)							
				1	2	3	4	5	6	7	8
1	Pd/ Al_2O_3 -sol	100	97	0.0	50.5	0.0	45.5	1.0	0.0	0.0	0.0
2	Pd/ TiO_2 -sol	100	98	0.0	50.5	0.0	47.0	1.0	2.0	0.0	0.0
3	Pd/ Nb_2O_5 -sol	100	95	0.0	45.9	0.0	16.7	23.6	6.6	0.0	0.0
4	Pd/ ZrO_2 -sol	100	86	0.0	48.0	0.0	1.0	37.0	0.0	0.0	0.0
5	Pd/ Nb_2O_5 -sol*	88	93	5.8	0.0	17.0	0.0	0.0	0.0	39.7	19.3

Reaction conditions: Reactant (62 mmol), decalin (15 mL), Pd/ Al_2O_3 -col (30 mg) Pd/ TiO_2 -col (30 mg), Pd/ Nb_2O_5 -col (30 mg), Pd/ ZrO_2 -col (30 mg), 503 K, 18 bar H_2 , 3h. *Reaction performed with 18 bar of N_2

For sol-immobilized Pd-based catalysts, the conversion of BPE thus starts with the hydrogenolysis of the $\text{C}_{\text{aliph}}\text{-O}$ bond catalyzed by the metal sites and by the production of phenol and toluene. Due to the small Pd particle size, phenol and toluene are rapidly hydrogenated to cyclohexanol and methylcyclohexane, respectively. For Pd/ Nb_2O_5 -sol and Pd/ ZrO_2 -sol catalysts, the significant formation of cyclohexane comes from the dehydration of cyclohexanol to cyclohexene by the acid sites of the support, followed by cyclohexene hydrogenation on metal sites. These two catalysts appear as especially active in the HDO process because of the presence of both small Pd particles and acid sites. Finally, because of the high activity of these catalysts for hydrogenation, BPE can be also partially hydrogenated over Pd particles to form cyclohexyl benzyl ether over Pd/ Nb_2O_5 -sol and Pd/ ZrO_2 -sol, but this reaction occurs in a limited extent.

An additional experiment was performed to confirm the activity for hydrogenation of Pd/Nb₂O₅-sol. The conversion of phenol was carried out in the same reaction conditions over the Pd/Nb₂O₅ catalysts prepared by impregnation and sol immobilization methods, using the same mass of catalyst. The Pd/Nb₂O₅-sol catalyst exhibited a higher phenol conversion than Pd/Nb₂O₅-imp (100 and 15%, respectively). For Pd/Nb₂O₅-sol, the main products formed were cyclohexane (83.5 %) and cyclohexanol (2.7 %), whereas cyclohexanone, an intermediate in the pathway from phenol to cyclohexanol, was produced over Pd/Nb₂O₅-imp. This result indicates that the Pd/Nb₂O₅-imp catalyst has a low activity for the hydrogenation of cyclohexanone to cyclohexanol.

These results reveal the high hydrogenation ability of the catalysts prepared by the sol immobilization method compared to those prepared by impregnation, and a combination between small metal Pd particles and acid sites is required for cyclohexane formation (deoxygenation product).

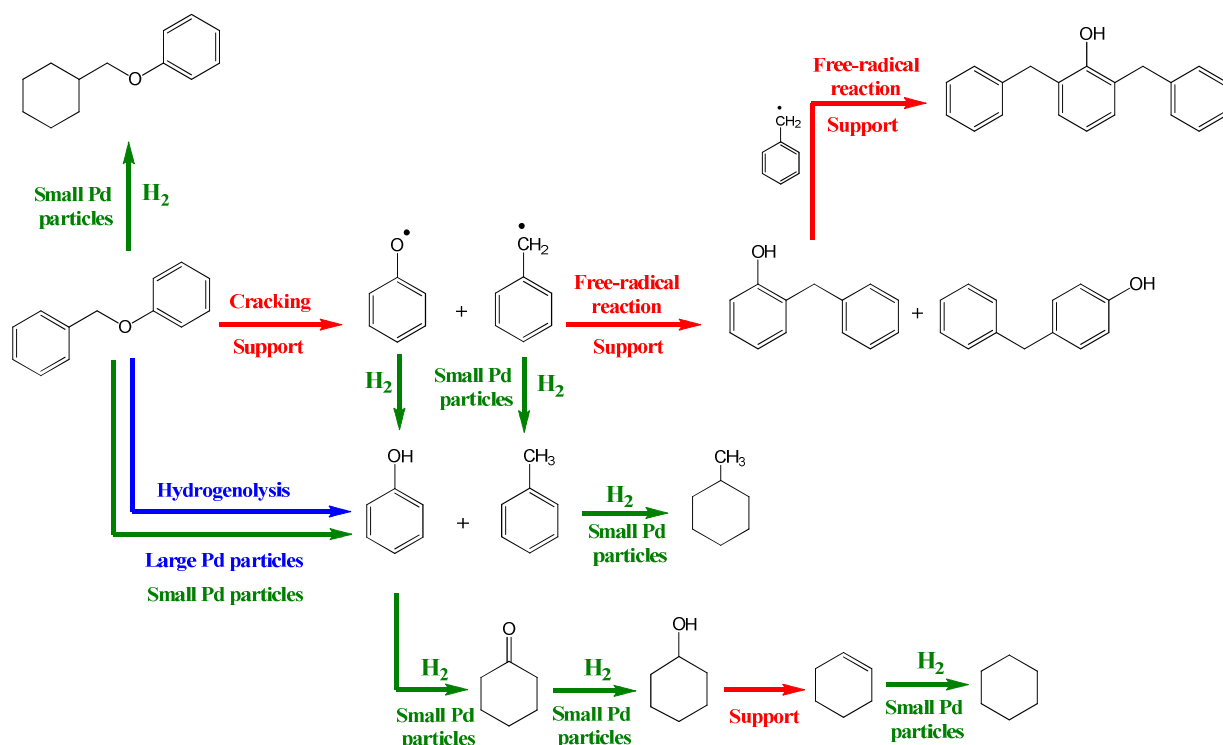
The lack of formation of alkylated products on the sol-immobilized catalysts could be due to: (i) the high rate of hydrogenolysis on these small metal particles, compared with the rate of cleavage of the C-O bond on the acid sites of the support; and (ii) the availability of hydrogen both for the hydrogenation of phenol and toluene, and for the hydrogenation of phenoxy and benzyl radicals, cutting the way to 2 and 4-BPH. To evaluate this hypothesis, the conversion of BPE was performed over Pd/Nb₂O₅-sol at 503 K, and under 18 bar of N₂ instead of H₂. The results are presented in Table 4, entry 5. In the absence of hydrogen, 88 % of BPE was converted to phenol, toluene, and alkylated products, which is the typical product distribution of the impregnated Pd/Nb₂O₅-imp catalyst. The hydrogenation properties of the metallic phase thus indirectly affect the formation of alkylated products. Not only an appropriate balance between metal sites and acidfunctions is required for the promotion of the last steps of the process leading to deoxygenation

(see above), but metals with a high hydrogenation ability and a large metal-support interface suppress the alkylation reaction by hydrogenating the radicals formed on the acid support. These important conclusions have not been reported before for this molecule.

These observations may explain the contradictory results obtained in the literature. The formation of alkylated products (2 and 4-BPH) was also observed for the conversion of BPE using a non-polar solvent (undecane) at 523 K and 40 bar of H₂ over Ni/SiO₂ and Ni/HZSM5 catalysts¹⁷. The alkylated products were preferentially formed over the acid support. However, alkylated products were not reported for Pd-Ni/ZSM5 (at 493 K, 20 bar of H₂ and *n*-hexane)²² or 2 wt.% Pt/TiO₂ (at 553 K, 10 bar H₂, in octane)¹⁹, more active for hydrogenation.

From the results obtained in our work, we propose the following network of reactions for the conversion of BPE over supported Pd-based catalysts in a non-polar solvent (decalin) (Scheme 1). The BPE molecule adsorbs either on the acid sites of the support and on the metallic Pd particles. Then, the cleavage of the C_{aliph}-O bond may proceed by two different reaction pathways: (i) cleavage of the C_{aliph}-O bond over acid sites of support, with the production of radicals followed by alkylation reaction and formation of dimers and trimers (Scheme 1, red route); or (ii) hydrogenolysis of the C_{aliph}-O bond promoted by the metallic Pd particles, producing toluene and phenol (Scheme 1, blue and green routes). On the catalysts possessing small Pd particles (catalysts prepared by sol immobilization method), toluene and phenol are further hydrogenated to methylcyclohexane and cyclohexanone/cyclohexanol, respectively. Then, cyclohexanol is dehydrated to cyclohexene when the support bears acid sites, and this is followed by the hydrogenation of cyclohexene to cyclohexane on the metallic particles (Scheme 1, green routes). The formation of alkylated products is inhibited due to the hydrogenation of the radicals formed by the metallic particles. Such a reaction network that takes simultaneously into account the

characteristics of the metal (particle size) and of the support (acidity) has never been proposed in the literature.



Scheme 1- Reaction pathway for the conversion of BPE over supported Pd-based catalysts.

Pressure and temperature effect for the conversion of BPE over Pd/Nb₂O₅-sol

Due to its high selectivity to deoxygenated products, Pd/Nb₂O₅-sol was selected to study the effect of hydrogen pressure and reaction temperature on the conversion of BPE. First, the reaction was performed at different hydrogen pressures (5, 10, and 18 bar of H₂) at 503 K, using decalin as solvent (Fig. 6).

Under 5 bar of H₂, toluene (23 %) and methylcyclohexane (21 %) on the one hand, and cyclohexanone (22 %) and cyclohexanol (14 %) on the other hand, were formed, indicating that phenol was completely hydrogenated to cyclohexanone/cyclohexanol after the cleavage of C_{aliph}-

O bond of BPE, while toluene was partially hydrogenated to methylcyclohexane. In addition, small amounts of cyclohexane (7 %) and bicyclohexyl-2-one (5 %), probably formed by the coupling between cyclohexanone and cyclohexene³⁷, were also produced. For this reaction time, 5 bar of hydrogen was thus not enough to perform the full hydrogenation of the hydrogenolysis products.

Increasing the H₂ pressure to 10 bar, toluene was completely transformed into methylcyclohexane, while cyclohexanone was totally hydrogenated into cyclohexanol. In addition, the yield of cyclohexane increased from 7 % to 29 % with the pressure increase.

At 18 bar of H₂, the yield of methylcyclohexane and cyclohexane slightly decreased compared to 10 bar H₂, while the yield of cyclohexanol increased. Furthermore, BPE was also partially hydrogenated. A high hydrogen pressure may thus be detrimental to the HDO process, because the hydrogenation of the BPE aromatic ring competes with the hydrogenolysis reaction, which leads to a lesser formation of deoxygenated products.

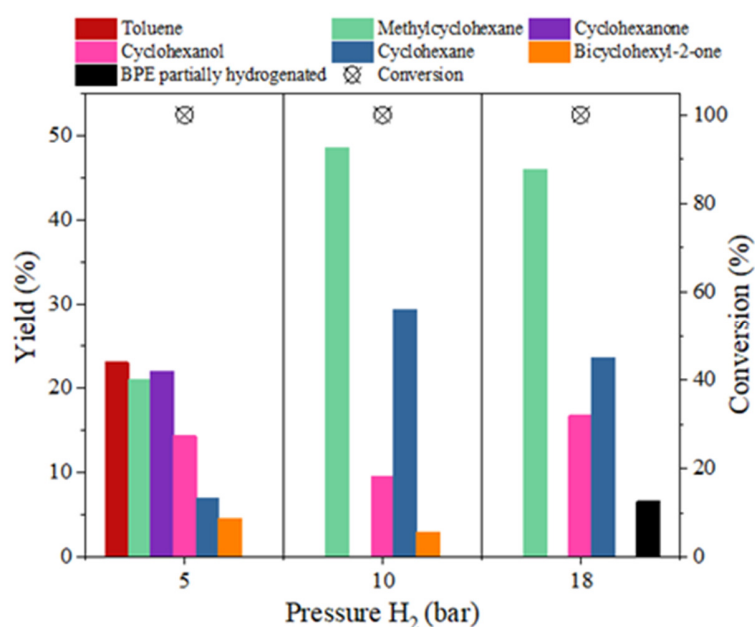


Figure 6- Conversion of BPE and product distribution at different H₂ pressures over Pd/Nb₂O₅-sol catalyst. Reaction condition: 62 mmol of BPE, Pd/Nb₂O₅-sol (30 mg), 503 K, in decalin, 3h.

Fig. 7 shows the conversion of BPE and product distribution for Pd/Nb₂O₅-sol, at different temperatures (373, 423, and 503 K) under 18 bar of H₂ in decalin. At 373 K, 64 % of BPE was converted to form toluene and phenol. Upon increasing the temperature to 423 K, complete conversion of BPE was achieved. Toluene was partially hydrogenated to methylcyclohexane, whereas phenol was completely hydrogenated to cyclohexanone and cyclohexanol, confirming that the reaction rate for the hydrogenation of phenol is higher than that for the hydrogenation of toluene. A further increase in the temperature to 503 K led to the complete hydrogenation of toluene to methylcyclohexane, while cyclohexanol was partially dehydrated to cyclohexene and converted to cyclohexane. Therefore, the hydrogenolysis reaction occurs at low temperature, but increasing the temperature to 423 K and above promotes the hydrogenation reactions. A further increase to 503 K favours the deoxygenation reaction. In addition, the partial hydrogenation of BPE was observed at all temperatures and the production of partially hydrogenated ethers remained roughly constant.

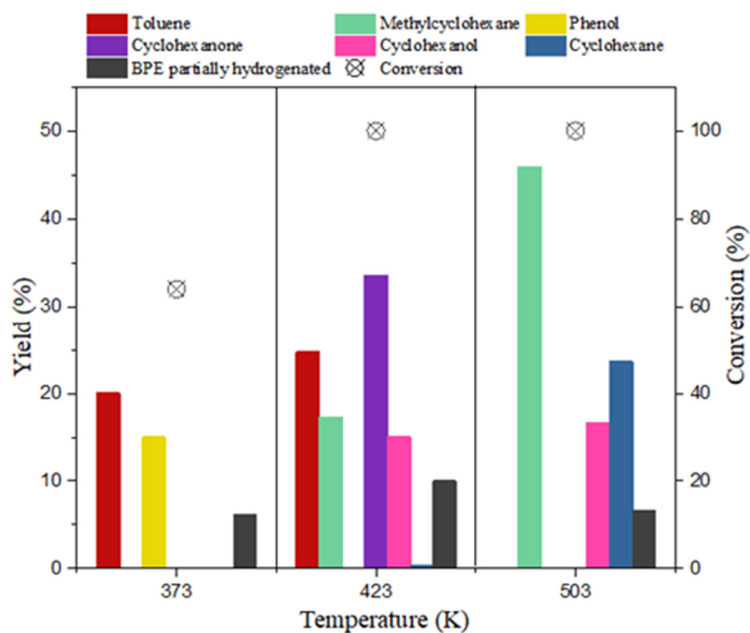


Figure 7-Conversion of BPE and product distribution at different reaction temperatures over Pd/Nb₂O₅-sol catalyst. Reaction condition: 62 mmol of BPE, Pd/Nb₂O₅-sol (30 mg), 18 bar of H₂, in decalin, 3h.

Conclusions

The conversion and the product distribution for the HDO of BPE are significantly affected by the Pd particle size as well as by the type of support. The large Pd particles, observed for impregnated catalysts, favored the hydrogenolysis of BPE into phenol and toluene; however, the subsequent hydrogenation did not occur. In parallel, the cleavage of C_{aliph}-O bond of BPE by the acid sites of support produced undesired aromatic dimers or trimers. The catalysts that exhibited the highest number of acid sites also presented the largest formation of 2 and 4-BPH. Over sol-immobilized catalysts, the smaller Pd particle size (< 4 nm) promoted the hydrogenation of phenol and toluene after C_{aliph}-O bond cleavage, to form cyclohexanone/cyclohexanol and methylcyclohexane, respectively. Due

to the high hydrogenation capacity of the small Pd particles, the intermediates formed in the presence of acid sites were quickly hydrogenated, and the formation of polyaromatics was suppressed. Furthermore, the deoxygenated product formed from the dehydration of cyclohexanol, cyclohexane, was only produced in the presence of Brønstedacid sites (niobia- and zirconia-supported catalysts). These results thus reveal that the HDO reaction of BPE and the competing reactions are strongly influenced by the particle size, the Brønstedacid sites and the presence of an important metal-support interface. Despite the importance of acid sites of support for deoxygenation, they also favor the formation of aromatic dimers and trimers. Therefore, an adequate balance between Bronsted acid sites and metallic sites containing small particles is required to promote the deoxygenation reaction to cycloalkanes.

The experimental conditions (reaction temperature and pressure) also affect the product distribution. Over the most active catalyst for HDO of BPE (Pd/Nb₂O₅ prepared by sol immobilization), low temperature (< 503 K) did not favor the formation of cyclohexane, and high hydrogen pressure (> 10 bar of H₂) led to some hydrogenation of the BPE aromatic rings, competing with the hydrogenolysis of BPE and consequently with the formation of cyclohexane. Intermediate pressure (10 bar) and high temperature (503 K) favors deoxygenation reaction.

Associated content

Supporting information

The supporting information is available free of charge

TEM images and the particle size distribution of Pd/SiO₂.imp(Figure S1), TEM images and the particle size distribution of Pd/Al₂O₃.imp (Figure S2), TEM images and the particle size distribution of Pd/Al₂O₃.col.(Figure S3), TEM images and the particle size distribution of Pd/TiO₂.imp (Figure S4), TEM images and the particle size distribution of Pd/TiO₂.col (Figure S5), TEM images and the particle size distribution of Pd/ZrO₂.imp (Figure S6), Chemical mapping of Pd/ZrO₂.col (Figure S7), TEM images and the particle size distribution of Pd/HZSM5 (Figure S8).

Acknowledgments

The Chevreul Institute (FR 2638) is thanked for its help in the development of this work through the ARCHI-CM project supported by the Ministère de l'Enseignement Supérieur de la Recherche et de l'Innovation, Région Hauts-de-France, the ERDF program of the European Union and the Métropole Européenne de Lille. This study was supported by the French government through the Programme Investissement d'Avenir (I-SITE ULNE / ANR-16-IDEX-0004 ULNE) managed by the Agence Nationale de la Recherche, CNRS. Métropole Européenne de Lille (MEL) and Region Hauts-de-France for the "CatBioInnov" project is also acknowledged. The authors would like to thank Ahmed Addad for the STEM images obtained on the electron microscopy facility of the Advanced Characterization Platform of the Chevreul Institute, Olivier Gardoll for the experiments of NH₃-TPD, and Jean-Charles Morin for the analysis by FTIR of pyridine adsorption. Fábio Bellot Noronha also thanks Fundação de Amparo à Pesquisa do Estado do Rio de Janeiro (FAPERJ – E-26/202.783/2017; 200.966/2021), Conselho Nacional de Desenvolvimento Científico e Tecnológico (CNPq - 303667/2018-4; 305046/2015-2; 302469/2020-6; 310116/2019-82) for financial support.

References

- (1) Araque-Marin, M.; Bellot Noronha, F.; Capron, M.; Dumeignil, F.; Friend, M.; Heuson, E.; Itabaiana, I.; Jalowiecki-Duhamel, L.; Katryniok, B.; Löfberg, A.; Paul, S.; Wojcieszak, R. Strengthening the Connection between Science, Society and Environment to Develop Future French and European Bioeconomies: Cutting-Edge Research of VAALBIO Team at UCCS. *Molecules***2022**, *27* (12), 3889. <https://doi.org/10.3390/molecules27123889>.
- (2) Ferraz, C. P.; Navarro-Jaén, S.; Rossi, L. M.; Dumeignil, F.; Ghazzal, M. N.; Wojcieszak, R. Enhancing the Activity of Gold Supported Catalysts by Oxide Coating: Towards Efficient Oxidations. *Green Chem.***2021**, *23* (21), 8453–8457. <https://doi.org/10.1039/D1GC02889H>.
- (3) Itabaiana Junior, I.; Avelar do Nascimento, M.; de Souza, R. O. M. A.; Dufour, A.; Wojcieszak, R. Levoglucosan: A Promising Platform Molecule? *Green Chem.***2020**, *22* (18), 5859–5880. <https://doi.org/10.1039/D0GC01490G>.
- (4) Tomishige, K.; Yabushita, M.; Cao, J.; Nakagawa, Y. Hydrodeoxygenation of Potential Platform Chemicals Derived from Biomass to Fuels and Chemicals. *Green Chem.***2022**, *24* (15), 5652–5690. <https://doi.org/10.1039/D2GC01289H>.
- (5) Shu, R.; Li, R.; Lin, B.; Wang, C.; Cheng, Z.; Chen, Y. A Review on the Catalytic Hydrodeoxygenation of Lignin-Derived Phenolic Compounds and the Conversion of Raw Lignin to Hydrocarbon Liquid Fuels. *Biomass Bioenergy***2020**, *132*, 105432. <https://doi.org/10.1016/j.biombioe.2019.105432>.
- (6) De, S.; Saha, B.; Luque, R. Hydrodeoxygenation Processes: Advances on Catalytic Transformations of Biomass-Derived Platform Chemicals into Hydrocarbon Fuels. *Bioresour. Technol.***2015**, *178*, 108–118. <https://doi.org/10.1016/j.biortech.2014.09.065>.

- (7) Zakzeski, J.; Bruijninx, P. C. A.; Jongerijs, A. L.; Weckhuysen, B. M. The Catalytic Valorization of Lignin for the Production of Renewable Chemicals. *Chem. Rev.***2010**, *110* (6), 3552–3599. <https://doi.org/10.1021/cr900354u>.
- (8) Song, W.; Lai, W.; Lian, Y.; Jiang, X.; Yang, W. Sulfated ZrO₂ Supported CoMo Sulfide Catalyst by Surface Exsolution for Enhanced Hydrodeoxygenation of Lignin-Derived Ethers to Aromatics. *Fuel***2020**, *263*, 116705. <https://doi.org/10.1016/j.fuel.2019.116705>.
- (9) Behling, R.; Valange, S.; Chatel, G. Heterogeneous Catalytic Oxidation for Lignin Valorization into Valuable Chemicals: What Results? What Limitations? What Trends? *Green Chem.***2016**, *18* (7), 1839–1854. <https://doi.org/10.1039/C5GC03061G>.
- (10) Rinaldi, R.; Jastrzebski, R.; Clough, M. T.; Ralph, J.; Kennema, M.; Bruijninx, P. C. A.; Weckhuysen, B. M. Paving the Way for Lignin Valorisation: Recent Advances in Bioengineering, Biorefining and Catalysis. *Angew. Chem. Int. Ed.***2016**, *55* (29), 8164–8215. <https://doi.org/10.1002/anie.201510351>.
- (11) Liu, Y.; Nie, Y.; Lu, X.; Zhang, X.; He, H.; Pan, F.; Zhou, L.; Liu, X.; Ji, X.; Zhang, S. Cascade Utilization of Lignocellulosic Biomass to High-Value Products. *Green Chem.***2019**, *21* (13), 3499–3535. <https://doi.org/10.1039/C9GC00473D>.
- (12) Wang, K.; Dayton, D. C.; Peters, J. E.; Mante, O. D. Reactive Catalytic Fast Pyrolysis of Biomass to Produce High-Quality Bio-Crude. *Green Chem.***2017**, *19* (14), 3243–3251. <https://doi.org/10.1039/C7GC01088E>.
- (13) Zhang, W.; Chen, J.; Liu, R.; Wang, S.; Chen, L.; Li, K. Hydrodeoxygenation of Lignin-Derived Phenolic Monomers and Dimers to Alkane Fuels over Bifunctional Zeolite-Supported Metal Catalysts. *ACS Sustain. Chem. Eng.***2014**, *2* (4), 683–691. <https://doi.org/10.1021/sc400401n>.

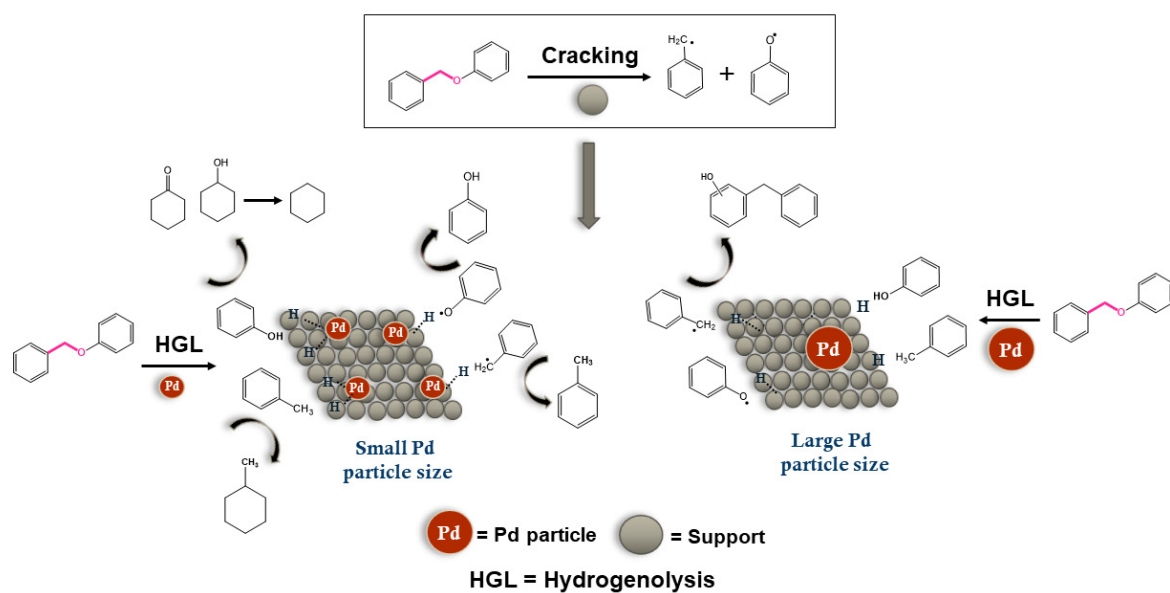
- (14) Yoon, J. S.; Lee, Y.; Ryu, J.; Kim, Y.-A.; Park, E. D.; Choi, J.-W.; Ha, J.-M.; Suh, D. J.; Lee, H. Production of High Carbon Number Hydrocarbon Fuels from a Lignin-Derived α -O-4 Phenolic Dimer, Benzyl Phenyl Ether, via Isomerization of Ether to Alcohols on High-Surface-Area Silica-Alumina Aerogel Catalysts. *Appl. Catal. B***2013**, *142–143*, 668–676. <https://doi.org/10.1016/j.apcatb.2013.05.039>.
- (15) Jung, K. B.; Lee, J.; Ha, J.-M.; Lee, H.; Suh, D. J.; Jun, C.-H.; Jae, J. Effective Hydrodeoxygenation of Lignin-Derived Phenols Using Bimetallic RuRe Catalysts: Effect of Carbon Supports. *Catal. Today***2018**, *303*, 191–199. <https://doi.org/10.1016/j.cattod.2017.07.027>.
- (16) Li, C.; Zhao, X.; Wang, A.; Huber, G. W.; Zhang, T. Catalytic Transformation of Lignin for the Production of Chemicals and Fuels. *Chem. Rev.***2015**, *115* (21), 11559–11624. <https://doi.org/10.1021/acs.chemrev.5b00155>.
- (17) He, J.; Lu, L.; Zhao, C.; Mei, D.; Lercher, J. A. Mechanisms of Catalytic Cleavage of Benzyl Phenyl Ether in Aqueous and Apolar Phases. *J. Catal.***2014**, *311*, 41–51. <https://doi.org/10.1016/j.jcat.2013.10.024>.
- (18) He, J.; Zhao, C.; Lercher, J. A. Ni-Catalyzed Cleavage of Aryl Ethers in the Aqueous Phase. *J. Am. Chem. Soc.***2012**, *134* (51), 20768–20775. <https://doi.org/10.1021/ja309915e>.
- (19) Shu, R.; Lin, B.; Wang, C.; Zhang, J.; Cheng, Z.; Chen, Y. Upgrading Phenolic Compounds and Bio-Oil through Hydrodeoxygenation Using Highly Dispersed Pt/TiO₂ Catalyst. *Fuel***2019**, *239*, 1083–1090. <https://doi.org/10.1016/j.fuel.2018.11.107>.
- (20) Guo, T.; Xia, Q.; Shao, Y.; Liu, X.; Wang, Y. Direct Deoxygenation of Lignin Model Compounds into Aromatic Hydrocarbons through Hydrogen Transfer Reaction. *Appl. Catal. A***2017**, *547*, 30–36. <https://doi.org/10.1016/j.apcata.2017.07.050>.

- (21) Zhao, C.; Lercher, J. A. Upgrading Pyrolysis Oil over Ni/HZSM-5 by Cascade Reactions. *Angew. Chem. Int. Ed.* **2012**, *51* (24), 5935–5940. <https://doi.org/10.1002/anie.201108306>.
- (22) Zhao, Y.-P.; Wu, F.-P.; Song, Q.-L.; Fan, X.; Jin, L.-J.; Wang, R.-Y.; Cao, J.-P.; Wei, X.-Y. Hydrodeoxygenation of Lignin Model Compounds to Alkanes over Pd–Ni/HZSM-5 Catalysts. *J. Energy Inst.* **2020**, *93* (3), 899–910. <https://doi.org/10.1016/j.joei.2019.08.002>.
- (23) Yao, G.; Wu, G.; Dai, W.; Guan, N.; Li, L. Hydrodeoxygenation of Lignin-Derived Phenolic Compounds over Bi-Functional Ru/H-Beta under Mild Conditions. *Fuel* **2015**, *150*, 175–183. <https://doi.org/10.1016/j.fuel.2015.02.035>.
- (24) Dou, X.; Li, W.; Zhu, C.; Jiang, X.; Chang, H.; Jameel, H. Cleavage of Aryl–Ether Bonds in Lignin Model Compounds Using a Co–Zn-Beta Catalyst. *RSC Adv.* **2020**, *10* (71), 43599–43606. <https://doi.org/10.1039/D0RA08121C>.
- (25) Roberts, V.; Fendt, S.; Lemonidou, A. A.; Li, X.; Lercher, J. A. Influence of Alkali Carbonates on Benzyl Phenyl Ether Cleavage Pathways in Superheated Water. *Appl. Catal. B.* **2010**, *95* (1–2), 71–77. <https://doi.org/10.1016/j.apcatb.2009.12.010>.
- (26) Kidder, M. K.; Britt, P. F.; Buchanan, A. C. Pyrolysis of Benzyl Phenyl Ether Confined in Mesoporous Silica. *Energy Fuels* **2006**, *20* (1), 54–60. <https://doi.org/10.1021/ef0502608>.
- (27) Thommes, M.; Kaneko, K.; Neimark, A. V.; Olivier, J. P.; Rodriguez-Reinoso, F.; Rouquerol, J.; Sing, K. S. W. Physisorption of Gases, with Special Reference to the Evaluation of Surface Area and Pore Size Distribution (IUPAC Technical Report). *Pure Appl. Chem.* **2015**, *87* (9–10), 1051–1069. <https://doi.org/10.1515/pac-2014-1117>
- (28) Pereira Costa, G.; Rafael, R. A.; Soares, J. C. S.; Gaspar, A. B. Synthesis and Characterization of ZnO–Nb₂O₅ Catalysts for Photodegradation of Bromophenol Blue. *Catal. Today* **2020**, *344*, 240–246. <https://doi.org/10.1016/j.cattod.2019.04.059>.

- (29) Guan, W.; Chen, X.; Hu, H.; Tsang, C.-W.; Zhang, J.; Lin, C. S. K.; Liang, C. Catalytic Hydrogenolysis of Lignin β -O-4 Aryl Ether Compound and Lignin to Aromatics over Rh/Nb₂O₅ under Low H₂ Pressure. *Fuel Process. Technol.***2020**, *203*, 106392. <https://doi.org/10.1016/j.fuproc.2020.106392>.
- (30) Martín Castro, A. M. Claisen Rearrangement over the Past Nine Decades. *Chem. Rev.***2004**, *104* (6), 2939–3002. <https://doi.org/10.1021/cr020703u>.
- (31) He, Y.; Yan, L.; Liu, Y.; Liu, Y.; Bai, Y.; Wang, J.; Li, F. Effect of SiO₂/Al₂O₃ Ratios of HZSM-5 Zeolites on the Formation of Light Aromatics during Lignite Pyrolysis. *Fuel Process. Technol.***2019**, *188*, 70–78. <https://doi.org/10.1016/j.fuproc.2019.02.004>.
- (32) Katritzky, A. R.; Allin, S. M.; Siskin, M. Aquathermolysis: Reactions of Organic Compounds with Superheated Water. *Acc. Chem. Res.***1996**, *29* (8), 399–406. <https://doi.org/10.1021/ar950144w>.
- (33) Zhao, C.; Lercher, J. A. Selective Hydrodeoxygenation of Lignin-Derived Phenolic Monomers and Dimers to Cycloalkanes on Pd/C and HZSM-5 Catalysts. *ChemCatChem***2012**, *4* (1), 64–68. <https://doi.org/10.1002/cctc.201100273>.
- (34) Villa, A.; Wang, D.; Veith, G. M.; Vindigni, F.; Prati, L. Sol Immobilization Technique: A Delicate Balance between Activity, Selectivity and Stability of Gold Catalysts. *Catal. Sci. Technol.***2013**, *3* (11), 3036. <https://doi.org/10.1039/c3cy00260h>.
- (35) Ferraz, C. P.; Zieliński, M.; Pietrowski, M.; Heyte, S.; Dumeignil, F.; Rossi, L. M.; Wojcieszak, R. Influence of Support Basic Sites in Green Oxidation of Biobased Substrates Using Au-Promoted Catalysts. *ACS Sustain. Chem. Eng.***2018**, *6* (12), 16332–16340. <https://doi.org/10.1021/acssuschemeng.8b03330>.

- (36) Monti, E.; Ventimiglia, A.; Garcia Soto, C. A.; Martelli, F.; Rodríguez-Aguado, E.; Cecilia, J. A.; Sadier, A.; Ospitali, F.; Tabanelli, T.; Albonetti, S.; Cavani, F.; Wojcieszak, R.; Dimitratos, N. Effect of the Colloidal Preparation Method for Supported Preformed Colloidal Au Nanoparticles for the Liquid Phase Oxidation of 1,6-Hexanediol to Adipic Acid. *Catalysts***2022**, *12* (2), 196. <https://doi.org/10.3390/catal12020196>.
- (37) Nimmanwudipong, T.; Runnebaum, R. C.; Tay, K.; Block, D. E.; Gates, B. C. Cyclohexanone Conversion Catalyzed by Pt/ γ -Al₂O₃: Evidence of Oxygen Removal and Coupling Reactions. *Catal Lett***2011**, *141* (8), 1072–1078. <https://doi.org/10.1007/s10562-011-0659-2>.

For Table of Contents Use Only



5

Reaction pathways for conversion of BPE over Pd supported catalysts with different Pd particle sizes.